Polymer-Nanocomposite Brush-like Architectures as an All-Solid Electrolyte Matrix

Soujanya Gowneni,[⊥] Kota Ramanjaneyulu,[⊥] and Pratyay Basak*

Nanomaterials Laboratory, Inorganic and Physical Chemistry Division, Council of Scientific & Industrial Research — Indian Institute of Chemical Technology (CSIR-IICT), CSIR — Network Institutes for Solar Energy (CSIR-NISE), Academy of Scientific and Innovative Research (AcSIR), Hyderabad-500 007, Andhra Pradesh, India. [⊥]S.G. and K.R. contributed equally to the study.

ABSTRACT Herein, we report on polymer-nanocomposites with brush-like architectures and evaluate their feasibility as an all-solid electrolyte matrix supporting Li^+-ion conduction. Showcased as a first example in the domain of electrolyte research, the study probes several key factors, such as (i) core morphology, (ii) surface modifiers/functionality, (iii) grafting length, and (iv) density of the brushes, and determines their role on the overall electrochemical properties of these nanostructured organic—inorganic hybrids. Nanostructured titania was synthesized *via* wet-chemical approaches using either controlled hydrolysis or hydrothermal methods. Exercising suitable control on reaction parameters led to well-defined morphologies/phases, such as nanoparticles, nanospindles, nanourchins, nanorods or nanotubes, in either anatase, rutile or mixed forms. Covalent anchoring on titania nanostructures was achieved using dopamine, gallic acid and glycerol as small organic moieties. A one-pot process of priming the available surface functional groups postmodification with isocyanate chemistry was followed by grafting polyethylene glycol monomethyl ethers of desired chain lengths. Finally, complexation with lithium salt yielded electrolyte compositions where the ethylene oxide (EO) fractions aid in ion-solvation with ease. The synthesized materials were characterized in detail employing XRD, TEM, DRS-UV, FTIR, micro-Raman, TG-DTA and DSC at each stage to confirm the products and ascertain the physicochemical properties. Comprehensive evaluation using temperature-step electrochemical impedance spectroscopy (EIS) of these brush-like nanocomposites provided crucial leads toward establishing a plausible physical model for the system and understanding the mechanism of ion transport in these all-solid matrices. The preliminary results on ionic conductivity (σ) obtained for some of the compositions are estimated to be within the range of $\sim 10^{-4}$ to 10^{-5} S cm^{-1} in the temperature window of the study that holds excellent promise for further improvement.

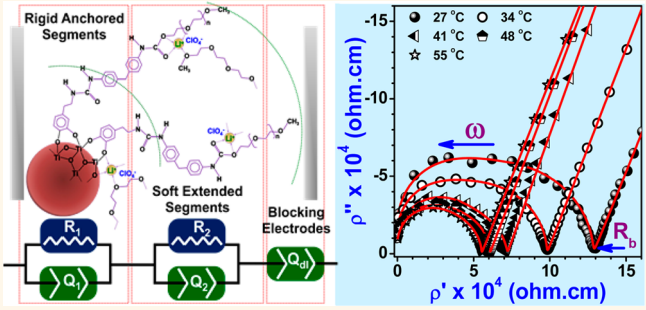

KEYWORDS: organic—inorganic hybrids · nanostructures · surface functionalization · polymer brushes · ionic conductivity

The target of achieving an ideal all-solid polymer electrolyte with appreciable Li^+-ion mobility has by far remained elusive and one of the most daunting challenges for researchers under the global new energy outlook, which has reintensified in recent years.[1−4] Early conceptualization by Wright[5−7] and Armand[8,9] is followed by several significant contributions over the years in the synthesis of new matrices, understanding the complex charge-transport properties, developing physical/theoretical models, and strategies to enhance material properties by notable research groups.[10−19] Nonetheless, the realization of a system that can provide ionic conductivity comparable to that of a liquid in an all-solid matrix has remained insurmountable. Overcoming the sluggish dynamics of macromolecular chains in absence of low molecular weight plasticization remains the major roadblock. One approach successfully employed is nanostructuring of the polymeric matrix using block copolymers so as to provide enough ion channels.[19−22] However, controlled synthesis of block copolymers with designer architecture for bulk usage do pose some applicability issues. In recent efforts from our group, a significant milestone in ionic conductivity, $\sigma \sim 10^{-4}$ S cm^{-1} at ambient was achieved for a new class of quasi-solid random semi-IPN systems notably without any external plasticization.[23,24]

* Address correspondence to pratyay@iict.res.in, pratyaybasak@gmail.com.

Received for review August 11, 2014 and accepted November 7, 2014.

Published online November 07, 2014
10.1021/nn504472v

Of the alternate techniques to enhance ionic transport, use of nanofillers that provide competitive interactions within the polymer matrix have gained popularity.[16,25−35] Yet, these nanocomposites impose the usual limitations of matrix homogeneity, loading amounts, agglomeration, and phase separation that add to concerns regarding reproducibility. Functionalization/surface modifications with small organic moieties like catechol on nanomaterial fillers do help to address few of the issues with a trade-off on the aspects of competitive interactions.[35] In concurrent research efforts evolving in other fields, such as advanced drug delivery, separation techniques, smart coatings and sensors, polymer grafted brush-like nanocomposites have shown very promising results.[36−39] Confinement, grafting density, brush length and molecule/ion diffusion all are key parameters that define interesting properties for such polymer nanocomposites (PNCs).[36,38] All these characteristics highlighted for the PNCs also uniquely position them to provide for an environment that is conducive for high segmental mobility, low crystallinity and enhanced interfacial interactions supporting fast ion-transport, envisaged as the prerequisites for an electrolyte matrix. To the best of our knowledge until date, however, this strategy has not been exploited in the field of electrolyte research. For the first time, we showcase the feasibility of adopting this approach in designing all-solid electrolyte matrices.

In the present investigation, we report on polymer-nanocomposites with brush-like architectures as a new class of an all-solid electrolyte matrix possessing reasonable Li^+-ion conductivity. The study attempts to probe several important factors that determine the overall physicochemical and electrochemical properties of these nanostructured organic−inorganic hybrids and evaluate their feasibility. To extend the proof of concept, these trials are restricted to the use of titania as the inorganic core and polyethylene glycol as the polymeric graft of our choice. Both the materials possess remarkable properties and have attracted immense attention owing to their unmatched industrial potential and technological viability.[11−13,40,41] Polyethylene glycol, by far, has the best ion solvation capability,[11−13] while titania in recent years has shown great promise as an anode material.[42,43] Key parameters explored herein, albeit with limited examples, are (i) morphology of the nanostructured core, (ii) chemistry of surface modifications (organic ligands/anchors), (iii) chain length of the graft and (iv) grafting density of the brushes. Well-defined nanoparticles, nanospindles, nanourchins, nanorods and nanotubes of titania were successfully synthesized to examine the role of morphology. Dopamine, gallic acid and glycerol were used as small organic moieties to achieve covalent anchoring on the titania nanostructures as well as generate reactive end groups on the surface. The modification was followed by a one-pot process of priming the surface with isocyanate chemistry (urethenation) and grafting polyethylene glycol of desired chain lengths. Finally, complexation with lithium salt yielded the electrolyte compositions. Throughout the effort, each step has been followed by detailed characterizations employing several techniques not only to confirm the formation of the targeted product but also to provide pertinent clues in understanding the overall behavior of these electrolyte matrices. The feasibility and potential of these brush-like nanocomposites are evaluated comprehensively employing temperature-step electrochemical impedance spectroscopy. Some interesting observations and crucial results indicate great promise to look beyond.

RESULTS AND DISCUSSION

The present report is an attempt to synthesize a new class of organic−inorganic hybrid polymer nanocomposite electrolyte with brush-like architectures to achieve an all-solid matrix possessing reasonable Li^+-ion conductivity. A detailed evaluation of the physicochemical and electrochemical properties of these polymer nanocomposite electrolyte brushes were initiated with the idea to optimize electrolyte compositions as a function of the nanostructure morphology, different functionality and the molecular weight of the polymeric components in the nanocomposite matrix. Variables possible for the present study, though intentionally kept limited within the large parameter space available, assessment of the key factors, such as (i) surface modifications/anchoring molecules, (ii) molecular weight/chain length of polymeric grafts, and (iii) role of morphology, all helped to understand the overall aspects that govern ion-conductivity behavior in these complicated systems.

Nanostructuring Titania. Synthesis of nanostructured titania (TiO_2), its crystalline phases (anatase, rutile, brookite), their potentially diverse industrial applicability and hence commercial importance are now well documented in literature.[41] With recent advances in synthetic strategies, appreciable control on the material morphology and phases formed can be achieved *via* relatively simpler wet-chemical routes notably even in absence of templates. In the present study, titania nanostructures of diverse morphologies and phase compositions were realized to rationalize two key factors, *i.e.*, the role of morphology and phase composition on the physicochemical and electrochemical behavior of the targeted hybrid nanocomposites as electrolytes. Albeit, the synthesis of TiO_2 were achieved employing some previously reported methodologies,[44−48] the confirmation on formation of nanostructures, phase and morphology desired was substantiated comprehensively before initiating further chemical modifications. The significant observations

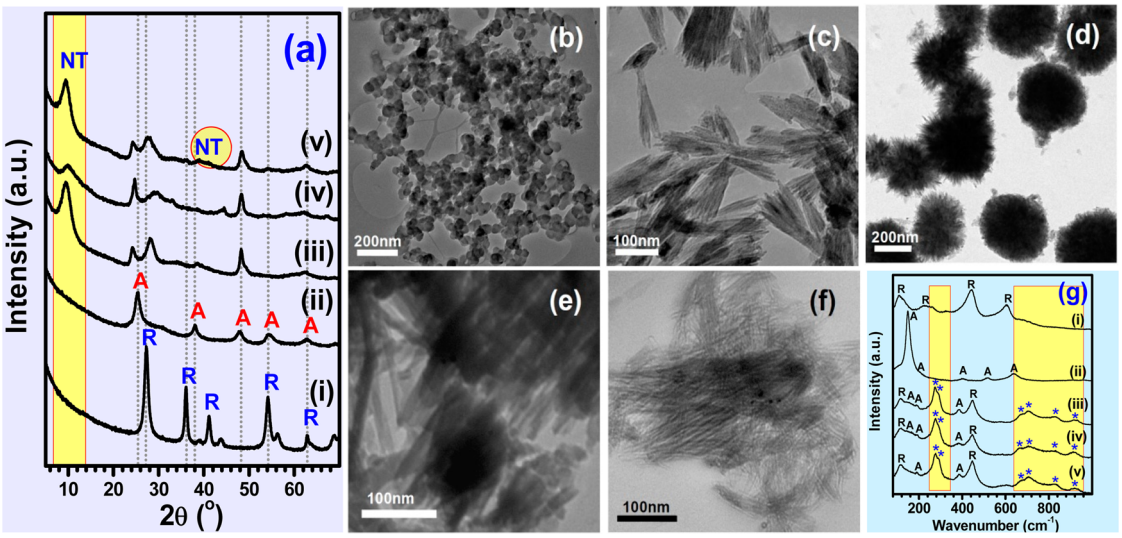

Figure 1. Stack plots of typical X-ray diffraction patterns: (a) different phases of titania (TiO_2) as synthesized (i) rutile, synthesized under acidic conditions at 80 °C by hydrothermal route, (ii) anatase, synthesized using hydrazine monohydrate (controlled hydrolysis) at room temperature, (iii) nanourchins (mixed phase) synthesized as in (i) followed by washing with basic solution, (iv) nanorods (mixed phase), obtained following digestion of rutile TiO_2 in 10 N NaOH autoclaved at 110 °C for 18h and (v) nanotubes (mixed phase), obtained following digestion of rutile TiO_2 in 10 N NaOH refluxed at 110 °C. Representative transmission electron microscopy images for different morphologies of nanostructured titania synthesized: (b) nanoparticles (T_{np}); (c) nanospindles (T_{ns}); (d) nanourchins (T_{nu}); (e) nanorods (T_{nr}); (f) nanotubes (T_{nt}); and (g) the corresponding Raman signals obtained for the samples in the same serial order confirming the formation and phases present.

and inferences drawn from the attempts are presented in Figure 1 which undoubtedly ascertains that a considerable control on the structure and phase can be exercised depending on the reaction conditions and the medium used. Typical X-ray diffraction patterns of different titania (TiO_2) phases synthesized is depicted in Figure 1(a) with detailed discussion provided in the Supporting Information. When the reaction medium is kept acidic (pH < 3), with presence of excess chloride-ions in the system, the synthesized phase is invariably pure rutile,[45,49] while the hydrazine monohydrate approach has been demonstrated to yield phase-pure anatase exclusively, even at room temperature.[44] Average crystallite sizes as determined from the fwhm of major peaks applying the Scherrer's equation for rutile is ~15−20 nm, while for anatase it is slightly smaller (~5−7 nm). Interestingly, the diffractograms Figure 1(a) (iii−v) for the synthesized materials showed obvious peak shifts along with an unmistakable low angle peak that indicated formation of layered sodium hydrogen titanates ($Na_yH_{2-y}Ti_nO_{2n+1}\cdot xH_2O$).[50−56]

Morphology of the synthesized nanostructures were evaluated employing transmission electron microscopy. Representative electron microscopy images for the five series of titania samples synthesized are presented in Figure 1(b−f). Noticeable distinction in the morphology achieved could be discerned with appreciable specificity to the synthetic route adapted. As evidenced, the morphologies observed relates well to certain geometric forms and have been appropriately coined as nanoparticles (T_{np}), nanospindles (T_{ns}), nanourchins (T_{nu}), nanorods (T_{nr}) and nanotubes (T_{nt}). Morphology of the final product is substantially dependent on the nucleation and growth (see Supporting Information for detailed discussion on proposed formation mechanisms).[57] The hydrazine monohydrate route leads to the formation of considerably monodisperse nanoparticles with average size distribution in the range of ~20−30 nm (Figure 1(b)). A chloride-ion excess environment (acidic medium), promotes preferential growth parallel to the *c*-axis, [110] direction,[45,49] facilitating the formation of rutile in spindle like geometries with an average aspect ratio of approximately (1:10) (Figure 1(c)). These rutile spindles/needles so formed, during the process of washing with basic aqueous solution, undergo partial phase change and agglomeration through self-assembly apparently seen as an overall urchin-like formation as evident from Figure 1(d). The formation of nanorods/nanotubes *via* a dissolution-reformation mechanism have been discussed by many authors,[56] and the aspect ratios for these nanotubes as seen in Figure 1(e) and (f), respectively, are estimated to be >20.

Structural confirmation of these nanostructures and morphologies was further substantiated employing Raman spectroscopy.[58−63] Figure 1(g) presents the stack-plots of micro-Raman signals obtained for the corresponding titania samples. The peaks at *ca.* 608, 440 and ~230 cm^{-1} in Figure 1(g):(i) could be assigned to A_{1g}, E_g and two photon scattering for the rutile phase of titania. Presence of a peak at ~110 cm^{-1} and a shoulder at ~688 cm^{-1} are signatures ascribed to A_{2u}/B_{1u} (optic mode acoustic vibrations) and A_{2g} (normally optically forbidden) modes, respectively,

implying the significantly small particle sizes. The peaks at 148 and 637 cm^{-1} are attributed to the E_g, 396 cm^{-1} to B_{1g} and 516 cm^{-1} to A_{1g} vibrational modes of phase-pure anatase TiO_2 in Figure 1(g):(ii). The strong signal at 148 cm^{-1} also signifies formation of ultrafine particles. In Figure 1(g):(iii−v), apart from the identified peaks for anatase and rutile, indicating formation of mixed phases, multiple vibrational bands at *ca*. 276, 290, 672, 705, 830 and 920 cm^{-1} are also prominently visible. These additional vibrational frequencies could be related to the presence of both sodium hydrogen titanate and hydrogen titanate as also inferred from the X-ray studies. Bands around 920 and 830 cm^{-1} can be assigned to Ti−O−Na and Ti−O−H symmetrical stretching modes with very short Ti−O distance in titanate structures.[58,59] The broad overlapped bands at ∼672 and ∼705 cm^{-1} can be attributed to the octahedral distortion in TiO_6^{2-}, as proposed for entrapped structural water/-OH groups during the dissolution-reformation mechanism.[60,61] The duplet symmetric stretching bands at *ca*. 290 and 276 cm^{-1} are symmetrical stretching modes for Ti−O−Na and Ti−O−H, respectively, indicating the presence of a layered structure in the lattice.[62,63] To sum up, the XRD, TEM and Raman studies corroborate each other significantly well and confirm the formation of a series of nanostructures, phase and desired morphology as targeted to initiate further chemical modifications.

Surface Functionalization and Modification of Nanostructured Titania. A series of polymer nanocomposites (PNCs) with brush-like architecture possessing titania as the nanostructured core and polyethylene glycol chains forming the bristles, were successfully synthesized. Schematic illustration of the different stages involved in a typical synthesis toward achieving the same is provided as Figure 2. Stable anchoring of the organic modifiers preferably through covalent linkages on the surface of nanostructures is a prerequisite criteria to proceed forward. Enediol ligands can effectively function as stable anchors on metal-oxides satisfying the considerable oxygen nonstoichiometry existing on the nanostructure surface. Low-temperature route for *in situ* functionalization of transition metal oxide *via* covalent linkage using a variety of enediol ligands, such as ascorbic acid, catechol, dopamine, alizarin, *etc*., has been previously reported by notable groups.[64−68] All of these studies have demonstrated the effectiveness of surface functionalization on the dispersion and colloidal stability of transition metal oxides in a wide range of solvents. In the present approach, we have effectively used a slightly modified procedure to functionalize the surface of titania nanostructures postsynthesis with three small organic moieties having multiple functionality. While the diol/acid groups are likely to anchor covalently on the metal oxide surface, the additional amine, acid or alcohol functionality is expected to be retained unbound and available for further chemical modifications.

Realization of the chemical alteration and confirmation for the nanostructures postfunctionalization was evidenced from XRD, mid-FTIR, micro-Raman, DR-UV and thermogravimetry studies. The details of the observations are compiled in the Supporting Information provided. The diffraction patterns for the titania nanospindles postfunctionalization with dopamine, gallic acid and glycerol show no perceptible changes in either their crystallinity index or phase formed (Figure S8). A favorable inference that could definitely be drawn is that neither the refluxing temperature nor the chemical attachments (new bonds) on the surface alter the parent nanostructures. The presence of all the signature peaks in mid-FTIR confirms covalent attachment/anchoring of the organic moieties.[69,70] Micro-Raman, however, generated weak signals, which were noticeably masked in the presence of metal-oxide core. Diffused reflectance studies in UV−vis region showed a considerable shift in the absorption band edge and perceptible broadening for the functionalized nanostructures.

Thermogravimetry studies (Figure S14) of functionalized rutile nanospindles confirmed on the aspects of both thermal stability as well as the approximate surface coverage attained postmodifications. The temperature onset (T_o) of thermal degradation is observed to be ∼200 °C, which indicates substantial stability of the bound organic components on the surface. As could be ascertained from the corresponding differential plots, apart from a negligible weight loss (∼1−2 wt %) up to 180 °C presumably because of moisture and/or bound water, the major loss of around 8−10 wt % is recorded within 200−400 °C. Attributed to the degradation and charring of small organic molecules, this stage also provides an estimation of the surface coverage, *i.e.*, grafting density achieved on the nanostructure surface. Though a quantitative thermogravimetric analysis on the products cannot be claimed in absence of proper control for validation, a fairly reasonable approximation within the error limits was arrived at following repeated runs on sizable number of samples. Estimates indicate that the organic functionalization achieved is in the range of $\sim 6 \times 10^{-4}$ mol/g of titania with an error of ±3%. Considering prior reports of quantitative analysis,[71,72] the results positively indicate that a substantially dense coverage on titania nanostructures has been successfully achieved.

Grafting of Polymeric Chains on Modified Nanostructures. Postfunctionalization and preliminary characterization of the titania nanostructures with dopamine, gallic acid and glycerol, free functional groups available on the surface was primed following isocyanate chemistry. Urethane chemistry has been successfully adapted in our ongoing efforts to design several new classes of

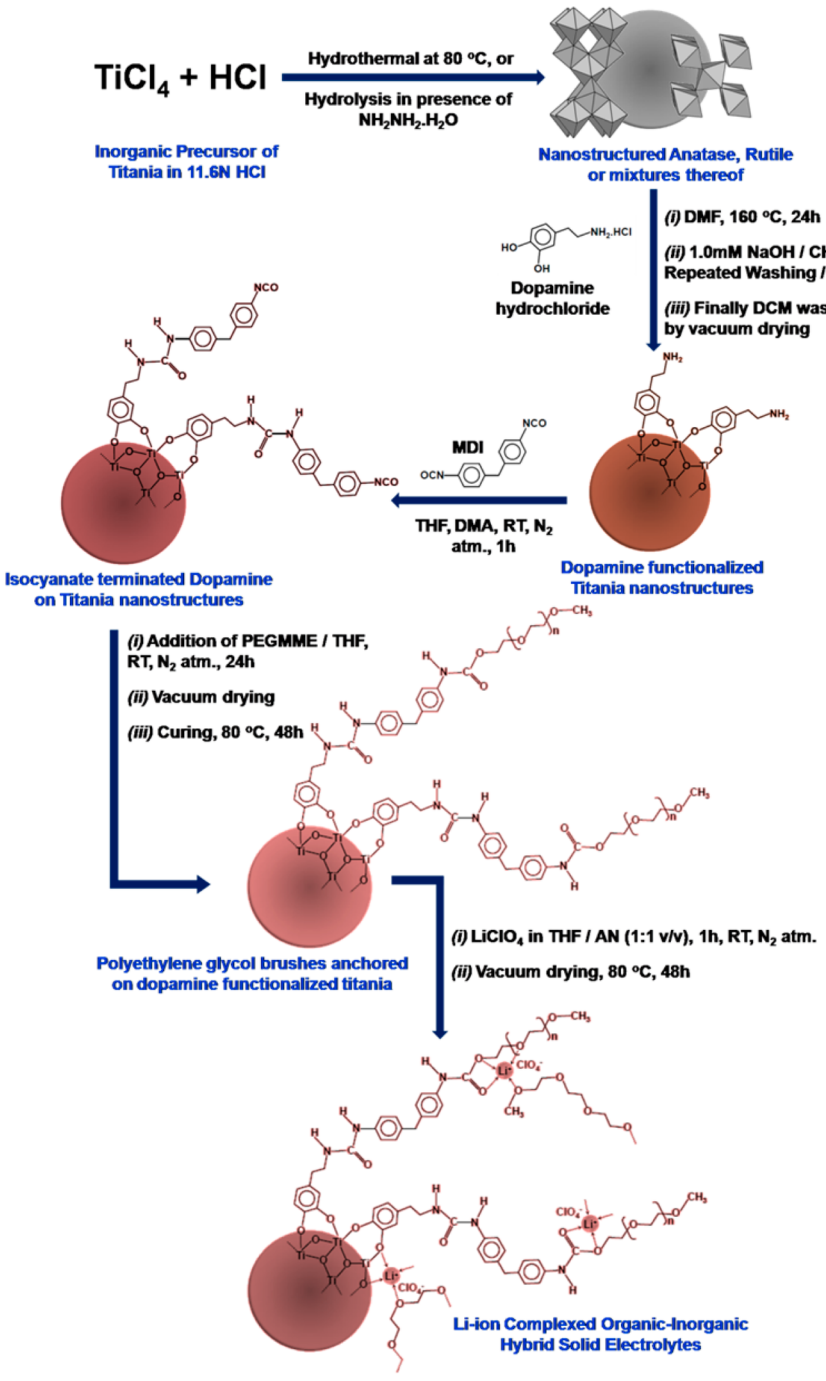

Figure 2. Representative scheme illustrating the synthetic route to obtain titania nanostructures, followed by their surface functionalization tethering dopamine, priming the surface with reactive isocyanate end groups using urethane chemistry, anchoring of polymeric chains of polyethylene glycol monomethyl ether to form grafted brush-like architectures and finally complexation with suitable lithium salts to achieve all solid organic−inorganic hybrid electrolytes.

solid/quasi-solid matrices as electrolytes.[23,24,35] The strategy involves reacting diisocyanates/polyisocyantes with reactive functional groups such as hydroxyls, amines and acids available on the modified titania to achieve an isocyanate terminated reactive shell. At this stage, oligomers/polymers with monofunctional end groups (-OH/-NH_2/-COOH) can be made to react with unreacted -NCO groups to obtain the desired grafts as depicted in the scheme (Figure 2). Finally, the polymer-nanocomposites were complexed with lithium salt ($LiClO_4$) to investigate the ion conduction behavior in all solid-state. The grafted chains of our choice in this present study are polyethylene glycol monomethyl ether (PEGMME) that possess excellent ion-solvation capability. Polyethylene glycols/polyethers are one of the most studied systems in the area of polymer electrolyte research and provides well-documented literature support to validate and

rationalize the findings. A range of molecular weight was used to study the effect of chain lengths on the physicochemical and electrochemical behavior of these systems when complexed with lithium salts.

Progress of the urethenation reaction although well-established is usually followed with mid-FTIR, where disappearance of the free isocyanate peak at *ca.* 2273 cm^{-1} is coupled with a concurrent appearance of a shoulder at *ca.* 1725 cm^{-1}.[23] The absence of the signature -NCO peak in the final products after curing at 80 °C and vacuum drying confirms the completion of the grafting reaction. Figure S17(A) highlights the composite mid-FTIR spectra in the region 2000−400 cm^{-1} for some representative hybrid systems complexed with $LiClO_4$. The ether (C−O−C) stretching region (1180−1000 cm^{-1}) with its characteristic band broadening owing to ion-complexation is quite emphatically visible in all the samples. The other noticeable bands observed are the urethane and ester C═O stretch at *ca.* 1700 cm^{-1}, free perchlorate anion at ∼637 cm^{-1}, all C−H bending and deformation vibrations along with the distinctive vibrational modes of the anchored organic ligands as assigned in the preceding section.

Thermal properties of these synthesized composites are assessed employing differential scanning calorimetry (DSC), Figure S17(B). The thermograms reveal an appreciably low glass transition temperature along with significant decrease in the degree of crystallinity for polyethylene glycol monomethyl ethers used for grafting. Evaluation summary of select samples used in the present study are provided in Table 1. For rutile nanospindles, a marked difference could be made out for the dopamine and gallic acid functionalization for the same set of polyethylene glycol grafts. A relatively higher T_g for dopamine functionalized nanostructures is probably observed because of the partial urchin-like self-aggregation for these nanospindles that occurs after NaOH/MeOH wash. Self-assembly can partly restrict the segmental motion of the grafted polymeric chain segments. Interestingly, in each set, cold crystallization and melting temperature peaks are also evidenced with increase in the molecular weight of the grafted polymers signifying minor presence of crystalline domains. The shift in T_c and T_m peaks toward higher temperature is also quite noticeable, presumably owing to the concomitant increase in intermolecular H-bonding. Effect of nanostructure morphology on the thermal properties at similar grafting lengths is also remarkable. The steady decrease in glass transition temperature with change in morphology from particles, spindles to tubular geometry signifies more wriggle room for the polymeric chain segments with increase in the aspect ratio of nanocomposite core. Evidently, the design strategy, synthetic approach, core morphology, grafting density, salt solvation properties and the thermal characteristics all complement each other satisfying some of the key prerequisites demanded of an ionically conducting all solid-state electrolyte matrix.

TABLE 1. Evaluation Summary on the Thermal Characteristics of the Various Hybrid Organic−Inorganic Polymer Nanocomposites Synthesized[a]

sample code	phase and morphology of the nanostructured core	T_g (°C)	T_c (°C)	T_m (°C)
Variation of Surface Functional Group and Grafted Chain Length of the Brush				
T_{ns}-DA-PEGMME-350	rutile, nanospindles	−47.5	—	—
T_{ns}-DA-PEGMME-550		−57.4	−17.1	8.5
T_{ns}-DA-PEGMME-750		−48.6	−2.6	17.6
T_{ns}-Ga-PEGMME-350		−70.1	—	—
T_{ns}-Ga-PEGMME-550[b]		−48.9	—	—
T_{ns}-Ga-PEGMME-750		−62.1	−44.7	20.6
Variation of Nanostructured Morphology				
T_{np}-Ga-PEGMME-550	anatase, nanoparticles	−41.2	—	—
T_{ns}-Ga-PEGMME-550[b]	rutile, nanospindles	−48.9	—	—
T_{nt}-Ga-PEGMME-550	mixed phase, nanotubes	−55.3	−16.2	9.3

[a] The glass transition temperature (T_g), cold crystallization temperature (T_c) and crystalline melting temperature (T_m), results were obtained by differential scanning calorimetry and analyzed using the software *Universal Analysis* provided by the TA Instruments. [b] The data has been reproduced in duplicate for ease of comparison.

Electrochemical Behavior of Organic−Inorganic Hybrid Nanocomposites. Ionic conductivity, mechanism of ion-conduction, relaxation times associated with ionic hopping, activation energy and microscopic polarization processes involved for the synthesized brush-like nanocomposites were assessed in considerable detail employing temperature-step electrochemical impedance spectroscopy (EIS). Prior inferences from extensive studies in our group on poly(ethylene oxide) based systems indicates that *ca.* 20 units of ethylene oxide (EO) accommodating one Li^+ is usually optimal for electrolyte compositions.[23,24,35] In the present investigation, we hence limit ourselves to the EO/Li mole ratio of 20 with lithium perchlorate solvated as an electrolyte. Evaluation of electrochemical impedance (Z) and the complex-plane Nyquist plots can be effectively done by creating a plausible physical model using a combination of distributed elements that best represents the real system under study.[73−77] Software simulations employing such models carried out on experimental data can aid in extracting several key information pertinent to the complex system response generated under the application of a sinusoidal field.

The graphical abstract provided represents a cartoon illustration of a realistic physical model of the all solid hybrid nanocomposite matrix under this study. The rationale for the model (see Supporting Information, Figure S18(a)) is based on an assumption of at least two microscopic domains (phases) that is believed to coexist: (i) the domains of grafted polymeric chain segments in the vicinity of nanoparticle surface (hard segments) and (ii) the domains of extended

polymeric chain segments (softer flexible region). The complexation of solvated Li^+-ions in these two domains understandably experience moderately different ion-polymer interactions.[35] Because of a possibility of competitive polymer−nanoparticle and ion−nanoparticle interactions, the transient Li^+-ion mediated cross-links are presumed to be more labile close to the nanoparticle surface. Nevertheless, the pinned down polymeric grafts aided by aromatic linkers (enediols and diphenyl diisocyanates) can provide considerable rigidity in and around this region. A trade-off is hence quite likely, which is possibly reflected in a slightly higher resistance observed at the nanoparticle−polymer interface (denoted by R_1). The extended polymeric PEGMME chain segments are comparatively more flexible and can provide for a least resistive path for ion transport (R_2). The associated capacitance in these two regions are indicated by two constant phase elements parallel to the resistors, as Q_1 and Q_2, respectively. The SS-blocking electrodes are aptly represented by a constant phase element, Q_{dl}, indicative of the double layer capacitance involved. The experimental data collected for all samples were normalized prior to the equivalent circuit fits for comparative appraisals.

Representative normalized complex-plane impedance plots (Nyquist plots) for the synthesized polymer grafted-nanotubes of TiO_2, T_{nt}-Ga-PEGMME-550, nanocomposite matrices complexed with $LiClO_4$ at different temperatures are provided alongside the graphical abstract and in Figure S18(b). A low frequency spike in combination with a semicircular arc observed in the mid/high- frequency region signifying the response of electrode-material interface and material bulk, are typical of such plots. Nonetheless, an apparently asymmetric nature of the depressed semicircular arc lends credence to our hypothesis that at least two microscopic domains are present within the matrix bulk. The signals are evidently merged presumably because of a very similar relaxation time associated with the ionic hopping events in both these domains. Software simulated model fits generated are depicted in the plots with overlapping solid red lines. The feasibility of our model and goodness of these fits is quite evident from the random distribution of residual data points along with concurrent fits to the bode plots (see Supporting Information, Figure S19 to Figure S22). Isolated contribution of resistance for designated domains estimated from these fits are provided in Table 2. As expected, with increase in temperature, the ion transport resistance in both the domains is seen to decrease steadily indicating faster dynamics associated with ionic hopping events.

Bulk resistance (R_b) of these hybrid nanocomposite systems were estimated from the intercepts of semicircular arcs/spike on the real axis of the Nyquist plots. Ionic conductivities determined for the systems as a function of temperature are presented as typical Arrhenius plots in Figure 3. Effects of molecular chain length of the polymeric graft as well as the molecular size/character of enediol ligand used are presented in the same plot for ease of comparison within or among the systems (Figure 3(a)). For all cases represented, nanostructure morphology is assumed to remain the same, *i.e.*, nanospindles. In the case of gallic acid anchored compositions, the bulk ionic conductivity varies within the range of 10^{-8} to 10^{-5} S cm^{-1} and an optimal graft length of polymeric brushes is demonstrated with PEGMME, M_n = 550 showing the best among the molecular weights 350, 550, and 750 studied. Interestingly, for the dopamine modified system, the ionic conductivity is seen to progressively increase with increasing chain length of the graft. Nevertheless, an apparent proximity of the estimated ion conductivity for M_n = 750 with that of $M_n \sim 550$ indicates that the increase would not be indeterminate and probably would show a critical molecular weight beyond the range of this particular study. Temperature dependence of ionic conductivity followed either classical Arrhenius equation ($\sigma = \sigma_0 \cdot \exp(-E_a/kT)$) or the empirical nonlinear V−T−F expression ($\sigma = \sigma_0 T^{-0.5} \cdot \exp(-E_a/k(T - T_0))$ proposed by Vogel−Tamman−Fulcher.[12,13] The estimated ionic conductivities at room temperature and at ~80 °C, activation energies associated with ionic hopping, V−T−F fitting parameters, temperatures where configurational entropies are assumed to be zero, all are summarized in Table 3. Overall, the electrolyte composition possessing dopamine functionalized titania with a PEGMME graft of $M_n \sim 750$ showed a better conductivity profile throughout the temperature window of study.

The inorganic core is expected to play an equally critical role with respect to the grafting density, interfacial interactions, ion diffusion lengths, associated H-bonding and crystallinity of the polymeric grafts. The significance of morphology for the nanostructured core selected on ionic conductivity of the system is separately assessed (Figure 3(b)). Three separate morphologyies, (i) nanoparticles, (ii) nanospindles and (iii) nanotubes surface modified with gallic acid and grafted with PEGMME, $M_n \sim 550$, were evaluated to demonstrate the rationale. Effect of grafting density is quite evident from the appreciably higher conductivity observed for nanoparticles and nanotubes. As inferred from the partial quantitative analysis employing TG-DTA (preceding section), the amount of organic components (weight %) estimated for all samples remain well within the limits of 8−10 wt % of titania. This implies that the number of effective covalent grafts almost remains unchanged within the acceptable error limits of detection. However, both the smaller nanoparticles as well as the nanotubular morphology with high aspect ratio arguably provides for higher surface area compared to that of nanospindles. Taking the

TABLE 2. Estimated Values for Individual Contribution of Distributed Elements Representing the Microphase Separation Isolated by Equivalent Circuit Simulation of the Hybrid Electrolyte Compositions[a]

	equivalent circuit model			power law fitting		
temp (°C)	$R_1 \times 10^4$ (Ω·cm)	$R_2 \times 10^4$ (Ω·cm)	$R_b \times 10^4$ (Ω·cm)	$\sigma_{0(UPL)} \times 10^{-6}$ (S cm^{-1})	$\tau_{(UPL)} \times 10^{-8}$ (sec)	$p_{(UPL)}$
			T_{ns}-DA-PEGMME-350, Nanospindles			
24	1090	377	1487	0.06	988	1.22
31	883	275	1130	0.09	749	1.20
38	417	216	628	0.16	510	1.22
45	329	60.3	384	0.26	320	1.16
52	193	33.5	222	0.45	144	0.95
			T_{ns}-DA-PEGMME-550, Nanospindles			
24	7.56	6.98	14.90	6.71	2.95	0.73
31	6.30	3.98	10.61	9.42	1.71	0.71
38	4.48	2.61	6.94	14.4	0.77	0.66
45	3.51	1.18	4.78	20.9	0.65	0.68
52	2.06	1.33	3.49	28.6	0.23	0.59
			T_{ns}-DA-PEGMME-750, Nanospindles			
24	6.41	3.58	10.19	9.81	3.89	0.81
31	4.27	3.35	7.87	12.7	2.14	0.74
38	3.98	1.33	5.23	19.1	0.73	0.64
45	2.30	1.01	3.35	29.8	0.18	0.53
52	1.28	0.98	2.38	42.0	0.02	0.39
			T_{np}-Ga-PEGMME-550, Nanoparticles			
27	14.3	13.0	28.32	3.53	23.4	0.67
34	9.19	7.82	17.69	5.65	15.0	0.72
41	2.78	6.70	9.61	10.4	9.48	0.80
48	2.92	2.30	5.37	18.6	4.79	0.77
55	2.66	1.01	3.73	26.8	2.97	0.77
			T_{ns}-Ga-PEGMME-550, Nanospindles			
23	323	104	497.51	0.20	2160	0.50
30	126	76.9	229.35	0.44	691	0.50
37	63.5	34.5	107.29	0.93	236	0.54
44	31.1	23.3	57.47	1.74	105	0.59
51	18.7	12.5	32.89	3.04	54.7	0.57
			T_{nt}-Ga-PEGMME-550, Nanotubes			
27	10.5	2.38	13.26	7.54	0.053	0.34
34	8.21	1.59	9.95	10.0	0.33	0.51
41	4.79	2.41	7.19	13.9	0.016	0.32
48	4.73	1.33	6.21	16.1	0.007	0.29
55	3.97	1.54	5.71	17.5	0.019	0.34

[a] The resistive contribution of the hard and soft domains for different surface modifiers, polymeric graft length and nanostructure core morphology are obtained from the fits to the experimental data collected at various temperatures.

geometric considerations into account, this possibly allows for additional wriggle room for the extended polymeric chain segments grafted on these surfaces alongside substantial ion−nanoparticle/polymer−nanoparticle interactions, which is reflected in their considerably higher ionic conductivities.

Noticeably for the systems, in particular gallic acid modified compositions, a two stage Arrhenius profile is observed with the second stage appearing beyond 50 °C. In absence of any evidence for the presence of crystalline domains as indicated in their thermal profiles (Figure S17(B) and Table 1), this transition can probably be related to extensive disordered H-bonding within the matrix. The assumption is reasonable considering the presence of carboxylic group of the small gallic acid molecule which may interact with the neighboring EO units. The second significant inference that can be drawn is the relatively higher conductivity at ambient temperatures for the surface grafted nanotubes and this may be attributed to the highly anisotropic nature of the core. A longer ion-diffusion length that can possibly be achieved on the tubular surface has been proposed in several studies albeit in a different context.[78,79] The skin of the nanomaterial-polymer domain can provide for a comparatively well-oriented ion channels for the Li^+-ions to skim through faster along the surface. With the increase in temperature, however, this effect is seemed

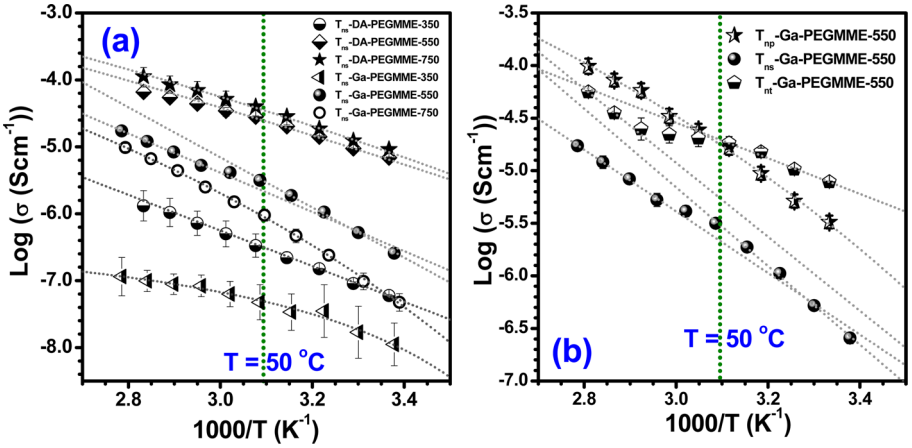

Figure 3. Typical log(σ) *vs* 1000/*T* Arrhenius plots depicting the dependence of ionic conductivity as a function of temperature showing (a) the effect of different functional group and chain length of the brush with titania nanospindles as the core, (b) the effect of different morphology of the titania nanostructures used. $LiClO_4$ at EO/Li = 20 is solvated in the composite electrolyte matrices. Dotted lines in the plot represents the extrapolated fits to the Arrhenius or Vogel–Tamman–Fulcher equation as found suitable in each case. The suitability of fits were ascertained comparing the R^2 and χ-values postfitting. The slope yields information on the activation energies of ionic hopping and ion-percolation events.

TABLE 3. Electrochemical Evaluation Summary for the Various Compositions of Organic–Inorganic Hybrid Polymer Nanocomposites Synthesized[a]

sample code	morphology	$\sigma_{RT} \times 10^{-6}$ (S cm^{-1})	$\sigma_{\sim 80°C} \times 10^{-5}$ (S cm^{-1})	E_{a1}[c] (eV)	log σ_0[c]	E_{a2}[c] (eV)	log σ_0[c]	log $\sigma_{0(VTF)}$[d]	$E_{a(VTF)}$[d] (eV)	$T_{0(VTF)}$[d] (K)
Variation of Surface Functional group and Grafted Chain Length of the Brush, -NCO/-OH Mole Ratio = 1.25										
T_{ns}-DA-PEGMME-350	nanospindles	0.06	0.16	0.85	1.73	—	—	—	—	—
T_{ns}-DA-PEGMME-550		7.94	7.94	—	—	—	—	1.87	0.262	70.3
T_{ns}-DA-PEGMME-750		9.33	12.59	—	—	—	—	1.40	0.195	109.5
T_{ns}-Ga-PEGMME-350		0.05	1.00	—	—	—	—	−4.80	0.019	245.4
T_{ns}-Ga-PEGMME-550[b]		0.26	1.21	1.19	6.07	0.93	3.41	—	—	—
T_{ns}-Ga-PEGMME-750		0.01	0.01	—	—	—	—	0.71	0.159	177.5
Variation of Nanostructured Morphology, -NCO/-OH Mole Ratio = 1.25										
T_{np}-Ga-PEGMME-550	nanoparticles	3.31	10.00	—	—	—	—	0.97	0.139	166.7
T_{ns}-Ga-PEGMME-550[b]	nanospindles	0.26	1.21	1.19	6.07	0.93	3.41	—	—	—
T_{nt}-Ga-PEGMME-550	nanotubes	7.94	5.62	0.54	0.55	1.12	5.636	—	—	—

[a] The bulk ionic conductivity at 27 and 80 °C, estimation of Arrhenius activation energies, as well as the fitting parameters for the Arrhenius and V–T–F equations are assessed as a function of functional moiety used to anchor the brushes to the surface of nanostructures, the chain length of the grafted oligomer and the effect of different nanostructure morphology on grafted density. [b] The data have been reproduced in duplicate for ease of comparison. [c] E_{a1} and E_{a2} are the activation energy from Arrhenius equation; $\sigma = \sigma_0 \cdot \exp(-E_a/kT)$ for two stage Arrhenius plots. [d] log $\sigma_{0(VTF)}$, $E_{a(VTF)}$ and $T_{0(VTF)}$ are parameters estimated from the V–T–F equation; $\sigma = \sigma_0 \cdot T^{-0.5} \exp\{-E_a/k(T - T_0)\}$.

to be neutralized and a crossover can be observed when compared to the profile of nanoparticle grafted matrix. Understandably, with increasing temperature the enhanced phonon vibrations along the nanotubular surface interferes with the channels orientation, thus interrupting the ease of ion-diffusion.[80,81] Above *ca.* 50 °C, the conventional mechanism of ion- percolation probably holds good and the smaller nanostructured core offers relatively lower resistance to ionic charge transport.

The spectroscopic plots of imaginary impedance as a function of frequency, conventionally called Debye plots, reveal information pertaining to the bulk relaxation dynamics of the systems. As presented in Figure 4(a), the single peak appearing at midfrequency region indicates a singular bulk relaxation time associated with ionic hopping. This lends support to the heavily superimposed response observed for two microscopic domains predicted in the Nyquist profiles. At the Debye peak maxima, an empirical relation, $\tau\omega = 1$, is satisfied and Lorentzian fits to these profiles (as shown in red lines) yield the peak position, f_{max}. The bulk relaxation times (τ_{peak}) for a typical system, *i.e.*, gallic functionalized titania nanospindles grafted with PEGMME 550 as shown are estimated in the range of 10^{-5} to 10^{-6} seconds. For systems which show higher bulk conductivities, the bulk relaxation dynamics are almost three to 5 orders of magnitude faster (10^{-8} to 10^{-10} s). With increase in test temperatures the peak position is observed to shift toward higher frequencies, implying faster relaxation processes that indicate ions are increasingly more labile and can follow the field with relative ease. Figure 4(b) shows the variation of real component of permittivity (ε') as a function of

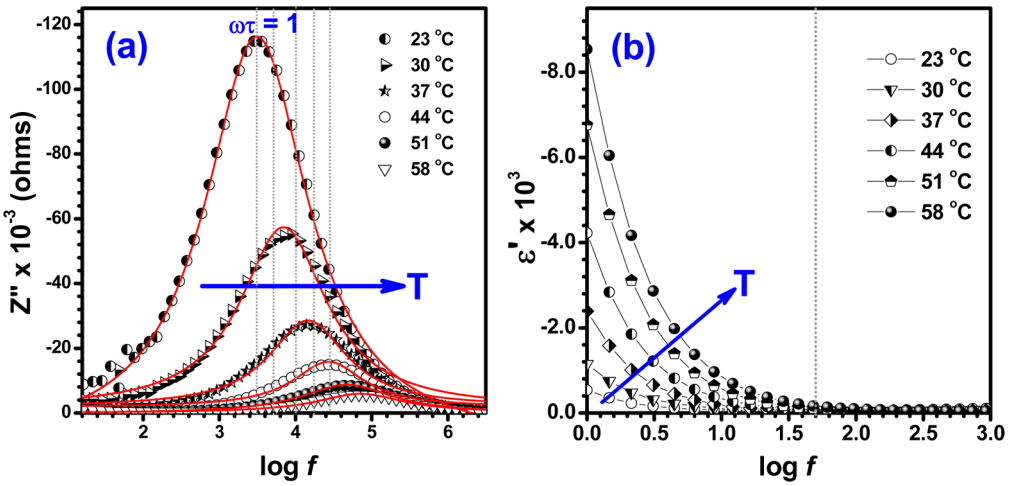

Figure 4. (a) Representative spectroscopic plot of imaginary impedance as a function of the log *f* (Debye plots) for the synthesized polymer grafted-TiO_2 nanocomposite electrolyte matrices, T_{ns}-Ga-PEGMME-550 containing $LiClO_4$ at EO/Li = 20. The Lorenztian peak fitting function (red lines) is used to determine the Debye peak position where the empirical relation; $\omega\tau = 1$ is satisfied and the estimated bulk relaxation time, τ indicates the time-scale of ion hopping events in the matrix. As observed, the peaks shift toward higher frequency indicating that the ions follow the field better aided by faster chain dynamics. (b) The permittivity of the sample at corresponding temperatures as a function of frequency indicating electrode−electrolyte polarization process at low frequency domain. As typical of any polar medium, the dielectric permittivity significantly increases with increase in temperature.

frequency. As with any polar medium, the dielectric permittivity is also seen to considerably increase with increasing temperature. Unlike our previous studies,[82] where two or more stages were observed, the present system shows a steady decrease of ε' with increasing frequency indicating contribution from a single polarization process. The low frequency domain is attributed to an electrode−electrolyte polarization contributing to a double layer capacitance at the interface. A steep fall in dielectric permittivity with increasing frequency can be associated with the inability of dipoles to rotate rapidly leading to a lag between the frequency of an oscillating dipole and that of the applied field. Thus, the flat response in the mid/high-frequency domain indicates no additional polarization processes, space-charge or otherwise arising within the matrix bulk. This observation signifies an apparent phase continuum with no charge build up at the interfaces of hard and soft polymeric segments of these nanocomposites and that the two identified domains are almost inseparable.

The frequency response of conductivity (real component) show a high degree of universality and can provide important clues in elucidating ion transport mechanisms as well as site-relaxation/reorganizations processes involved in the matrix bulk. The real component of conductivity, $\sigma'(\omega)$ was calculated from the impedance data using the equation[73,83] $\sigma'(\omega) = Z'(\omega)/k[(Z'(\omega))^2 + (Z''(\omega))^2]$, where k is the cell constant in cm. Figure 5 shows real component of conductivity, $\sigma'(\omega)$ as a function of log *f* at different temperatures for two characteristic morphologies (nanoparticles and nanospindles) of T_{nx}-Ga-PEGMME-550/$LiClO_4$ at various temperatures. Three distinct zones can be clearly identified in the plots: (I) a electrode−electrolyte interface at low frequency, (II) the frequency independent plateau in midfrequency zone and (III) a high frequency dispersion of $\sigma'(\omega)$. A steep increase in conductivity in low frequency region is attributed to polarization effects at the electrode and electrolyte interfaces, where the double-layer capacitance drops very rapidly with increase in frequency. In the intermediate range, conductivity is found to be almost frequency independent (the plateau region) and is equal to bulk *dc*-conductivity ($\sigma(0) = \sigma_{dc}$). In high frequency region, ion-conductivity progressively increases and shows frequency dispersion beyond a critical percolation frequency, ω_c (where $\sigma'(\omega) = 2\sigma(0)$), and is dependent on the material and temperature. This steep increase in $\sigma'(\omega)$ at high frequencies can be attributed to correlated ionic motions in these all solid nanocomposite electrolytes.

For highly disordered systems such as glasses and polymers this universality has been demonstrated very effectively by several major groups, in particular by Roling *et al.*,[84,85] Furukawa *et al.*[86,87] and Di Noto *et al.*[83,88,89] The jump−relaxation model proposed by Jonscher that explains the transport phenomenon, dielectric relaxation and their dependence on thermal activation is universally applicable to a wide class of materials.[90] An equivalent expression of the power law modified by Crammer *et al.*[91] $\sigma'(\omega) = \sigma(0)\cdot[1+(\tau\omega)^p]$ helps explain the frequency dependence of ionic transport process taking into account the coulombs interaction between mobile ions. The power law exponent, "*p*", denotes the ratio of initial site relaxation time of ionic hopping, τ' (= $1/r_f$, where r_f is the rate of forward jump) to that of back-hop relaxation time,

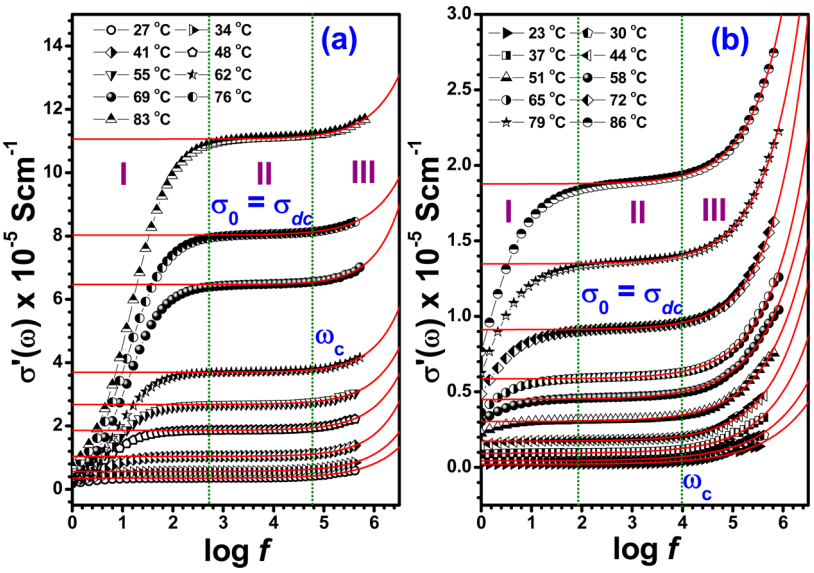

Figure 5. Real component of conductivity, $\sigma'(\omega)$ as a function of log *f* at different temperatures: (a) nanoparticles, T_{np}-Ga-PEGMME-550 and (b) nanospindles, T_{ns}-Ga-PEGMME-550 complexed with $LiClO_4$ at EO/Li mole ratio = 20. Three distinct zones can be clearly identified: electrode−electrolyte interface (I), the frequency independent plateau region (II) and the high frequency dispersion due to correlated motions of ions along with the polymer-chain dynamics (III). Red lines are the fit to the modified power law, $\sigma'(\omega) = \sigma_0(1 + (\tau\omega)^p$ for the experimental data in the region II and III, where "τ" is the bulk relaxation time for a successful hopping event and "*p*" is the power law exponent signifying the site-reorganization rates related to backward/forward hop ($p = \tau'/\tau^* = r_b/r_f$).

τ^* (= $1/r_b$, where r_b is the back-hop rate) and can help predict the nature of predominant charge carriers associated with successful jumps,[82,83,91] while the relaxation time, τ, is related to the initial site-relaxation time (τ') and signifies the bulk relaxation rate for the system under study. The real components of conductivity data ($\sigma'(\omega)$) for region II and III are fitted with the modified power law expression as depicted by the red lines in Figure 5 and the parameters generated are summarized in Table 2. As can be compared, the estimated $\sigma(0)$ as well as τ-values are in good agreement with the σ_{RT} determined from Nyquist plots and bulk relaxation rates arrived at from the Debye plots (τ_{peak}). Dependence of log τ as a function of temperature (1000/*T*) is depicted in Figure S23(a). That the relaxation process is thermally activated is quite evident from these plots. The trends show a steady decrease indicating a faster relaxation kinetics aiding the ionic transport at higher temperatures. However, the most noticeable highlight of these simulated fits are the estimated power law exponent, "*p*". In general, under an external field the process of charge migration depends on the rate of successful hop from the occupied sites to an available empty site. The host medium reorganization involves both the sites, *i.e.*, the one that was coordinating the ion as well as the site that would possibly accept that ion. Thus, during an ion hopping event, the correlated events will necessitate a shift in the potential cage along with geometrical/spatial rearrangement of the host. In most cases of polymer electrolytes, the cations are usually coordinated by transient cross-links, and hence the hopping events are usually associated with the Li^+-ion. Anions on the other hand remain in close proximity. Since, $p = \tau'/\tau^*$ = back-hop rate (r_b)/site-relaxation (r_f), the fact that "*p*" observed is <1 throughout the temperature window of study for most compositions is quite significant (Figure S23(b)). The ratio indicates that the rate of successful jumps are appreciably high and the charge transport for these hybrid nanocomposite systems are predominantly cationic in nature ($t_c > t_a$). That the ions are the majority charge carriers ($t_i \gg t_e$) is evidenced directly from *dc*-polarization studies on these system (see Supporting Information, Figure S24).

CONCLUSIONS

A series of organic−inorganic polymer-nanocomposites with brush-like architectures were successfully synthesized and evaluated for their Li^+-ion conductivity and showcase their feasibility as a new class of an all-solid electrolyte matrix. The key factors investigated to determine their role on the overall electrochemical properties of these nanostructured organic−inorganic hybrids are (i) core morphology, (ii) surface modifiers/functionality, (iii) grafting length, and (iv) density of the brushes. Titania nanostructures of diverse morphologies and phase compositions were realized to rationalize two key factors, *i.e.*, the role of morphology and phase composition on the physicochemical and electrochemical behavior of the targeted hybrid nanocomposites as electrolytes. Confirmation on formation of nanostructures, phase and morphology desired was substantiated comprehensively before initiating further chemical modifications. Exercising suitable

control on reaction parameters lead to well-defined nanostructured morphologies/phases, such as nanoparticles, nanospindles, nanourchins, nanorods or nanotubes of titania in either anatase, rutile or mixed forms, which was validated using XRD, TEM and micro-Raman studies. Covalent anchoring on the titania nanostructures postsynthesis was achieved successfully using dopamine, gallic acid and glycerol as small organic moieties. While the diol/acid groups anchored covalently on the metal oxide surface, the additional amine, acid or alcohol functionality is retained unbound and available for further chemical modifications. The chemical attachment was confirmed using FTIR, micro-Raman, DRS-UV and thermogravimetry. A reasonable approximation within the error limits estimates the organic functionalization achieved is in the range of $\sim 6 \times 10^{-4}$ mol/g of titania. A favorable inference that could definitely be drawn is that neither the refluxing temperature nor the chemical attachments (new bonds) on the surface apparently alter the parent nanostructures as confirmed from XRD patterns. A one-pot process of priming the available surface functional groups postmodification with isocyanate chemistry was followed by grafting polyethylene glycol monomethyl ethers of desired chain lengths. Complexation with lithium salts yielded electrolyte compositions where the ethylene oxide (EO) fractions aids in ion-solvation. The progress of urethenation reaction is followed using mid-FTIR, and thermal properties of these synthesized composites were assessed employing DSC. A steady decrease in the glass transition temperature with change in morphology from particles, spindles to tubular geometry for similar number of surface grafts signifies more wriggle room for the polymeric chain segments with increase in the aspect ratio of the nanocomposite core.

Comprehensive evaluation of ionic conductivity, mechanism of ion-conduction, relaxation times associated with ionic hopping, activation energy, microscopic polarization processes involved for the synthesized brush-like nanocomposites were assessed in considerable detail employing temperature-step electrochemical impedance spectroscopy (EIS). In-depth analysis of the experimental data provided crucial leads toward establishing a plausible physical model of the system and understand the mechanism of ion transport in these new class of all-solid matrices. Bulk ionic conductivity (σ) obtained for some of the organic–inorganic hybrid compositions are estimated to be within the range of $\sim 10^{-4}$ to 10^{-5} S cm^{-1} in the temperature window of the study and holds excellent promise for further improvement. Apparently, the approach met two important objectives simultaneously, *i.e.*, (a) covalent surface modifications with good coverage, excellent anchoring and stability with considerable ease and effectiveness of processing; (b) the additional reactive functional groups facilitate tethering polymeric grafts on the nanostructures as the bristles. The architecture helps to retain the low glass transition temperature and mechanical stability desired of the polymers (polyethylene glycols in this case) while increasing the amorphous nature of the ion-conduction pathways within a solid matrix. Thus, the design strategy, synthetic approach, core morphology, grafting density, salt solvation properties and thermal characteristics all complement each other, satisfying some of the key prerequisites and evidently conducive to rapid ion-transport in an all solid-state electrolyte matrix. To sum up, these reassuring and encouraging results favorably indicate the potential of nanostructured hybrid electrolytes and open up an option to look beyond.

EXPERIMENTAL SECTION

Materials. Titanium tetrachloride ($TiCl_4$) (Merck), ethanol (EtOH) (SRL), hydrochloric acid (HCl) (Rankem), hydrazine monohydrate ($N_2H_4.H_2O$) (Rankem), sodium hydroxide (NaOH) (RANKEM) and Milli-Q deionized water (18.2 MΩ) were used for the synthesis of titania nanostructures. Dopamine hydrochloric acid (DA.HCl) (Aldrich), gallic acid (Aldrich), glycerol (Aldrich), methanol (MeOH) (RANKEM), dichloromethane (DCM) (RANKEM) and dimethylformamide (DMF) (RANKEM) were used for surface functionalization of the synthesized titania nanostructures. Diphenylmethane diisocyanate (MDI) (Merck), polyethylene glycol monomethyl ether (PEGMME, M_n = 350, 550, 750) (Aldrich), *N*,*N*-dimethylaniline (DMA) (Sigma), tetrahydrofuran (THF), and acetonitrile (AN), (RANKEM), lithium perchlorate ($LiClO_4$) (Aldrich), were used for further modification of the funclionalized nanostructures to form the organic–inorganic hybrid brushes and their electrolyte compositions. The PEGMME, THF and acetonitrile used were dried prior to the synthesis of nanocomposites.

Synthesis of Titania Nanoparticles. The synthesis of titania (TiO_2) nanoparticles in this attempt was achieved with slight modification to a previously reported procedure from our group.[44] In a typical synthesis, 5 mL of titanium tetrachloride ($TiCl_4$) was dissolved in 10 mL of concentrated 11.6 N HCl to form a stock solution. The solution was then slowly added to an ethanol–deionized water (1:1 v/v) mixed solvent system (~200 mL) under stirring conditions over a period of 30 min. To this reactant mix, an aqueous solution of hydrazine monohydrate ($NH_2NH_2.H_2O$) was added dropwise from a buret under vigorous stirring to attain a final solution pH of ~8. Initial formation of a cloudy colloidal white precipitate followed by rapid dissolution process finally transformed into a persistent white colloidal suspension. The reaction mixture was left under stirring condition with intermittent addition of a drop or two of hydrazine monohydrate solution to maintain the pH at ~8, for another 12 h at room temperature and finally allowed to settle. The solution was centrifuged to obtain the white precipitate, which was resuspended in DI water followed by centrifugation. These steps were repeated several times until the supernatant of washing was found free of chloride ions. The material was oven-dried at 60 °C and lightly grinded in a mortar to finally obtain a powdery white product of titania nanoparticles as inferred following routine characterizations. The materials so synthesized are coded as "T_{np}" in the text.

Synthesis of Titania Nanospindles[45]**.** In a typical synthesis, 2.5 mL of titanium tetrachloride ($TiCl_4$) is added to 10 mL of

concentrated hydrochloric acid (11.6 N, HCl) to prepare an acidic stock solution of titanium tetrachloride. The solution is slowly added dropwise to 50 mL of deionized water, under constant stirring over a period of 30 min. The transparent solution was transferred into an autoclave and hydrothermally treated at 80 °C for 6 h. After the completion of the reaction time the autoclave was allowed to cool down to room temperature to retrieve a milky white colloidal solution. The suspension was centrifuged, and the white precipitate so obtained was resuspended in deionized water, centrifuged and decanted repeatedly until the washings were free of chloride ions. Finally, the centrifuged product was oven-dried at ~60 °C and lightly grinded to obtain a fine white powder. The materials so synthesized are denoted as "T_{ns}" in the text. Detailed characterization employing XRD, Raman and TEM was carried out to confirm the metal-oxide formation, phase and morphology.

Synthesis of Titania Nanourchins. In a similar approach as described for the nanospindles, the precursor and reaction conditions were maintained the same. After completion of reaction, however, the procedure for washing was slightly modified. The white colloidal suspension obtained was washed with 0.1 N aqueous NaOH followed by centrifugation to quickly neutralize the excess acid. Finally, the product was washed with deionized water until a neutral pH was attained for the washings. The material dried at 60 °C is coded as "T_{nu}" in the text.

Synthesis of Titania Nanorods. The nanorod morphologies were achieved following a strategy reported recently by Armstrong *et al.*[46] In a typical procedure, 500 mg of preformed titania nanospindles (T_{ns}) synthesized as described in the preceding section is digested in 10 N NaOH at 120 °C for 18 h under hydrothermal conditions. Following the completion of reaction time, the precipitate obtained was subjected through repeated wash cycles using a 0.1 N aqueous HCl followed by centrifugation and finally deionized water until a neutral pH was attained for the washings. The material dried at 60 °C is coded as "T_{nr}" in the text.

Synthesis of Nanotubes. Following a procedure described by Kasuga *et al.*,[47,48] the nanospindles of titania were refluxed in 10 N NaOH solution for 48 h under mechanical stirring at 110 °C. Subsequent to the digestion process the product was centrifuged and washed several times with 0.1 N aqueous HCl followed by deionized water until a neutral pH was attained. Finally, the product dried in oven at 60 °C and coded as "T_{nt}" was characterized in detail to confirm the metal-oxide formation, phase and morphology.

Dopamine Functionalization of TiO_2 Nanostructures Postsynthesis. Dopamine hydrochloride (DA.HCl) was used for surface functionalization of the synthesized TiO_2 nanostructures. In a typical reaction, 1 g of TiO_2 was vacuum-dried at 150 °C for 2 h to activate the surface followed by a quick addition of 30 mL of dimethylformamide (DMF) under warm conditions (~60 °C) to obtain a relatively homogeneous white suspension. Addition of 0.1 g of DA.HCl to this suspension showed an immediate change in its color to brown. The reaction mixture was allowed to reflux under continuous stirring for 24 h at 160 °C under nitrogen atmosphere. The resulting brown suspension after aging was repeatedly washed with 1.0 mM solution of sodium hydroxide in methanol for several times to free the amine and centrifuged. Finally, the material was washed with methylene dichloride (DCM) twice to remove any physisorbed dopamine. The product was left to dry at room temperature followed by oven drying at 60 °C and characterized. These dopamine functionalized titania nanoparticles will be hereafter designated as "T_{nx}-DA" in the text.

TiO_2 Nanostructures Functionalized with Gallic Acid/Glycerol. The synthesis of gallic acid/glycerol functionalized titania nanostructures was achieved following a similar protocol as described in the preceding section. The resulting brown/white suspension after aging was centrifuged, and the precipitate was thoroughly washed with only methylene chloride several times and oven-dried at 60 °C before characterization. The products are coded as "T_{nx}-Ga" and "T_{nx}-Gly" for the gallic acid and glycerol functionalized titania nanostructures, respectively.

Grafting Polymeric Chains on Surface Modified Nanostructures. In a slightly modified approach to our earlier reports,[23,24,35] the free amine/acid/alcohol functional groups available on the surface modified nanostructures were primed with diisocyanate using simple urethane chemistry. In a typical reaction, 1 g of "T_{nx}-Y" was reacted with ~1.25 equiv of 4,4′-diphenylmethane diisocyanate (MDI) with respect to 1 equiv of functional groups in the presence of a room temperature catalyst *N*,*N*-dimethylaniline (DMA) in THF for 1 h under inert atmosphere to form an isocyanate functionalized surface on the nanostructured core of choice. At this stage, the reaction vessel was charged with 1 equiv of polyethylene glycol monomethyl ether (M_n ~ 350, 550, 750 as desired), and the reaction was allowed to continue for another 24 h. Finally, the THF was evaporated under reduced pressure, vacuum-dried, and the solid product so obtained was allowed to cure at 80 °C for another 48 h. The products are accordingly coded as "T_{nx}-Y-PEGMME-*z*" in the text, where "*x*" hints the nanostructure morphology, "Y" is the ligand used for covalent anchoring on titania surface and "*z*" is the molecular weight of the PEGMME used.

Preparation of All-Solid Hybrid Nanocomposite Electrolyte Compositions. To achieve electrolyte compositions, hybrid polymer-nanocomposites synthesized were resuspended in a THF/AN (1:1 v/v), and desired amount of lithium perchlorate was added under inert atmosphere and allowed to solvate. The excess solvent was evaporated under reduced pressure and vacuum-dried at 80 °C prior to carrying out the physicochemical and electrochemical characterizations. The $LiClO_4$ concentration was maintained at EO/Li mole ratio of 20 with respect to the PEGMME used for grafting.

Characterization. The X-ray diffraction (XRD) patterns of the synthesized materials were collected on a PANalytical Empyrean equipped with Pixel 3D detector. Transmission electron microscope (TEM) (Philips Tecnai FEI F12, operating at 120 kV) was used to investigate the morphology of synthesized nanostructures. The micro-Raman and Fourier transform infrared (FTIR) spectroscopy were performed on a Horiba Jobin-Yvon LabRam HR spectrometer and Bruker ALPHA-T instrument, respectively. Diffused reflectance spectra were recorded on a UV−vis−NIR Varian Cary 5000 spectrometer while the thermal properties of the functionalized nanomaterials were assessed using thermogravimetry, TA Q50 analyzer and differential scanning calorimetry, Q200 (TA Instruments). The alternating current (*ac*-) electrochemical impedance spectroscopy (EIS) for the synthesized organic−inorganic hybrid polymer-nanocomposite electrolytes of various compositions was carried out on a Zahner Zennium electrochemical workstation controlled by Thales Operational Software. The data were collected following a frequency sweep through 1 Hz to 4 MHz range at an alternating potential with a RMS-amplitude of ±10 mV across the OCV of the assembled cells. The synthesized samples were invariably vacuum-dried overnight and handled inside a JACOMEX glovebox (Argon atmosphere) to assemble in spring loaded Swagelok-cells for carrying out the measurements. Additional details pertaining to the characterization protocols, sample preparation techniques, experimental setup employed and analysis are provided in the Supporting Information.

Conflict of Interest: The authors declare no competing financial interest.

Acknowledgment. S.G. acknowledges the Department of Science & Technology (DST), India, and CSIR-IICT for financial assistance in the form of DST-Inspire Junior Research Fellowship (GAP-0389). K.R. acknowledges Council of Scientific and Industrial Research (CSIR), India, for financial assistance in the form of Senior Research Fellowship (SRF). P.B. duly acknowledges the strong support of DST-Ramanujan Fellowship (GAP-0248), MNRE-CSIR TAPSUN Project on Dye Sensitized Solar Cells (*Dye*Cell: GAP-0366) and CSIR TAPSUN Project on Innovative Solutions for Solar Energy Storage (*Store*Solar: NWP-0056) for the grants received. The authors sincerely appreciate the encouragements and considerable help received from Dr. S.V. Manorama, Dr. K.V.S.N. Raju, Dr. R.K. Rana and Dr. R. Narayan during the course of this investigation.

Supporting Information Available: Additional details on the characterization protocols, sample preparation techniques, experimental setup employed, all relevant data and additional

discussions on the formation of nanomaterials/nanocomposites probed by XRD, TEM, FTIR, micro-Raman, DSC, TG-DTA, DLS particle size estimation, along with EIS studies, actual equivalent circuit fittings of Nyquist/Bode plots, residuals obtained postfitting, plots of relaxation time and power law exponents as a function of temperature and *dc*-polarization tests. This material is available free of charge *via* the Internet at http://pubs.acs.org.

REFERENCES AND NOTES

1. *International Energy Outlook Report May 27, 2009*; Office of Integrated Analysis and Forecasting, U.S. Department of Energy: Washington, D.C., 2009; http://www.eia.doe.gov/oiaf/ieo/index.html, 20585.
2. Lewis, N. S. Towards Cost-Effective Solar Energy Use. *Science* **2007**, *315*, 798–801.
3. Graetzel, M. Photoelectrochemical Cells. *Nature* **2001**, *414*, 338–344.
4. Alamgir, M.; Moulton, R. D.; Abraham, K. M. In *Primary and Secondary Lithuim Batteries*; Abraham, K. M., Salomon, M., Eds.; Electrochemical Society: Pennington, NJ, 1991.
5. Fenton, D. E.; Parker, J. M.; Wright, P. V. Complexes of Alkali Metal Ions with Poly(ethylene oxide). *Polymer* **1973**, *14*, 589–589.
6. Wright, P. V. Electrical Conductivity in Ionic Complexes of Poly(ethylene oxide). *Br. Polym. J.* **1975**, *7*, 319–327.
7. Wright, P. V. An Anomalous Transition to a Lower Activation Energy for DC Electrical Conduction above the Glass-Transition Temperature. *J. Polym. Sci., Polym. Phys. Ed.* **1976**, *14*, 955–957.
8. Armand, M. B.; Chabagno, J. M.; Duclot, M. J. *Extended Abstracts, Second International Conference on Solid Electrolytes, St. Andrews, Scotland*; Elsevier: Amsterdam, 1978.
9. Armand, M. B.; Chabagano, J. M.; Duclot, M. J. In *Fast Ion Transport in Solids: Electrodes Electrolytes*; Vashishta, P., Mundy, J. N., Shenoy, G. K., Eds.; Elsevier: Amsterdam, 1979; p 131.
10. Ratner, M. A. In *Polymer Electrolyte Reviews*; MacCallum, J. R., Vincent, C. A., Eds.; Elsevier Applied Science: New York, 1987; Vol. 1.
11. Ratner, M. A.; Shriver, D. F. Ion Transport in Solvent-Free Polymers. *Chem. Rev.* **1988**, *88*, 109–124.
12. Gray, F. M. In *Solid Polymer Electrolytes—Fundamentals and Technological Applications*; VCH: Weinhem, Germany, 1991.
13. Gray, F. M. In *Polymer Electrolytes*; The Royal Society of Chemistry: Cambridge, U.K., 1997.
14. Zhang, Z.; Fang, S. Ionic Conductivity and Physical Stability Study of Gel Network Polymer Electrolytes. *J. Appl. Polym. Sci.* **2000**, *77*, 2957–2962.
15. Alamgir, M.; Abraham, K. M. In *Lithium Batteries—New Materials, Developments and Perspectives*; Pistoia, G., Ed.; Elsevier: Amsterdam, 1994.
16. Leo, C. J.; Rao, G. V. S.; Chowdari, B. V. R. Studies on Plasticized PEO—Lithium Triflate—Ceramic Filler Composite Electrolyte System. *Solid State Ionics* **2002**, *148*, 159–171.
17. Kim, Y. T.; Smotkin, E. S. The Effect of Plasticizers on Transport and Electrochemical Properties of PEO-based Electrolytes for Lithium Rechargeable Batteries. *Solid State Ionics* **2002**, *149*, 29–37.
18. Kato, Y.; Hasumi, K.; Yokoyama, S.; Yabe, T.; Ikuta, H.; Uchimoto, Y.; Wakihara, M. Polymer Electrolyte Plasticized with PEG-Borate Ester having High Ionic Conductivity and Thermal Stability. *Solid State Ionics* **2002**, *150*, 355–361.
19. Hallinan, D. T.; Balsara, N. P. Annual Review of Materials Research. *Polym. Electrolytes* **2013**, *43*, 503–525.
20. Singh, M.; Odusanya, O.; Wilmes, G. M.; Gomez, E. D.; Patel, A. J.; Chen, V. L.; Park, M. J.; Eitouni, H. B.; Fragouli, P.; Iatrou, H.; *et al.* Effect of Molecular Weight on the Mechanical and Electrical Properties of Block Copolymer Electrolytes. *Macromolecules* **2007**, *40*, 4578–4585.
21. Gomez, E. D.; Panday, A.; Feng, E. H.; Chen, V.; Stone, G. M.; Minor, A. M.; Kisielowski, C.; Downing, K. H.; Borodin, O.; Smith, G. D.; *et al.* Effect of Ion Distribution of Conductivity of Block Copolymer Electrolytes. *Nano Lett.* **2009**, *9*, 1212–1216.
22. Wanakule, N. S.; Panday, A.; Mullin, S. A.; Glann, E.; Hexamer, A.; Balsara, N. P. Ionic Conductivity of Block Copolymer Electrolytes in the Vicinity of Order-Disorder and Order-Order Transitions. *Macromolecules* **2009**, *42*, 5642–5651.
23. Bar, N.; Ramanjaneyulu, K.; Basak, P. Quasi-Solid Semi-Interpenetrating Polymer Networks as Electrolytes: Part I. Dependence of Physicochemical Characteristics and Ion Conduction Behavior on Matrix Composition, Cross-Link Density, Chain Length between Cross-Links, Molecular Entanglements, Charge Carrier Concentration, and Nature of Anion. *J. Phys. Chem. C* **2014**, *118*, 159–174.
24. Bar, N.; Basak, P. Quasi-Solid Semi-Interpenetrating Polymer Networks as Electrolytes: Part II. Assessing the Modes of Ion-Ion and Ion-Polymer Interactions Employing the mid-FTIR Vibrational Spectroscopy. *J. Phys. Chem. C* **2014**, *118*, 10640–10650.
25. Gurevitch, I.; Buonsanti, R.; Teran, A. A.; Gludovatz, B.; Ritchie, R. O.; Cabana, J.; Balsara, N. P. Nanocomposites of Titanium Dioxide and Polystyrene-Poly(ethylene oxide) Block Copolymers as Solid-State Electrolytes for Lithium Metal Batteries. *J. Electrochem. Soc.* **2013**, *160*, A1611–A1617.
26. Croce, F.; Appetechi, G. B.; Persi, L.; Scrosati, B. Nanocomposite Polymer Electrolytes for Lithium Batteries. *Nature* **1998**, *394*, 456–458.
27. Jayathalaka, P. A.; Dissanayake, M. K. L.; Albinsson, I.; Mallander, B.-E. Effect of Nano-Porous Al_2O_3 on Thermal, Dielectric and Transport Properties of the $(PEO)_9LiTFSI$ Polymer Electrolyte System. *Electrochim. Acta* **2002**, *47*, 3257–3268.
28. Best, A. S.; Adebarhr, J.; Jacobsson, P.; MacFarlane, D. R.; Forsyth, M. Microscopic Interactions in Nanocomposite Electrolytes. *Macromolecules* **2001**, *34*, 4549–4555.
29. Mercniek, M.; Zalewska, A.; Zukowska, G.; Wieczorek, W. Composite Electrolytes Based on Low Molecular Weight Polyglycols. *Solid State Ionics* **2000**, *137*, 1175–1179.
30. Scrosati, B.; Croce, F.; Panero, S. Progress in Lithium Polymer Battery R&D. *J. Power Sources* **2001**, *100*, 93–100.
31. Ana, M. A. S.; Benavente, E.; Romero, P. G.; Gonzalez, G. Poly(acrylonitrile)—Molybdenum Disulfide Polymer Electrolyte Nanocomposite. *J. Mater. Chem.* **2006**, *16*, 3107–3113.
32. Wieczorek, W.; Lipika, P.; Ukoswka, G. Z.; Wycislik, H. Ionic Interactions in Polymeric Electrolytes Based on Low Molecular Weight Poly(ethylene glycol)s. *J. Phys. Chem. B* **1998**, *102*, 6968–6974.
33. Xiong, H. M.; Liu, D. P.; Zhang, H.; Chen, J. S. Polyether-Grafted SnO_2 Nanoparticles Designed for Solid Polymer Electrolytes with Long-Term Stability. *J. Mater. Chem.* **2004**, *14*, 2775–2780.
34. Xiong, H.-M.; Wang, Z.-D.; Xie, D.-P.; Cheng, L.; Xia, Y.-Y. Stable Polymer Electrolytes Based on Polyether-Grafted ZnO Nanoparticles for All-Solid-State Lithium Batteries. *J. Mater. Chem.* **2006**, *16*, 1345–1349.
35. Shah, Md. S. A. S.; Basak, P.; Manorama, S. V. Polymer Nanocomposites as Solid Electrolytes: Evaluating Ion—Polymer and Polymer—Nanoparticle Interactions in PEG-PU/PAN Semi-IPNs and Titania Systems. *J. Phys. Chem. C* **2010**, *114*, 14281–14289.
36. Choi, J.; Hore, M. J. A.; Clarke, N.; Winey, K. I.; Composto, R. J. Nanoparticle Brush Architecture Controls Polymer Diffusion in Nanocomposites. *Macromolecules* **2014**, *47*, 2404–2410.
37. Choi, J.; Dong, H.; Matyjaszewski, K.; Bockstaller, M. R. Flexible Particle Array Structures by Controlling Polymer Graft Architecture. *J. Am. Chem. Soc.* **2010**, *132*, 12537–12539.
38. Kumar, S. K.; Jouault, N.; Benicewicz, B.; Neely, T. Nanocomposites with Polymer Grafted Nanoparticles. *Macromolecules* **2013**, *46*, 3199–3214.
39. Dang, A.; Hui, C. M.; Ferebee, R.; Kubiak, J.; Li, T.; Matyjaszewski, K.; Bockstaller, M. R. Thermal Properties of Particle Brush

Materials: Effect of Polymer Graft Architecture on the Glass Transition Temperature in Polymer-Grafted Colloidal Systems. *Macromol. Symp.* **2013**, *331*−*332*, 9–16.
40. Tryk, D. A.; Fujishima, A.; Honda, K. Recent Topics in Photoelectrochemistry: Achievements and Future Prospects. *Electrochim. Acta* **2000**, *45*, 2363–2376.
41. Linsebigler, A. L.; Guangqan, L.; Yates, J. T. Photocatalysis on TiO_2 Surfaces: Principles, Mechanisms, and Selected Results. *Chem. Rev.* **1995**, *95*, 735–758.
42. Wallace, G. G.; Chen, J.; Mozer, A. J.; Forsyth, M.; MacFarlane, D. R.; Wang, C. Nanoelectrodes: Energy Conversion and Storage. *Mater. Today* **2009**, *12*, 20–27.
43. Kalyanasundaram, K., Ed.; *Dye-Sensitized Solar Cells*; CRC Press: Boca Raton, FL, 2010; p 57.
44. Manorama, S. V.; Reddy, K. M.; Basak, P.; Nisha, C. K.; Reddy. C. V. G. Simultaneous Preparation of Nanocrystalline Anatase Titanium Dioxide Powder and Hydrazine Monohydrochloride, Comprises Adding Hydrazine Monohydrate Solution Drop Wise to Acidic Aqueous Solution of Titanium Tetra Chloride. US2005106095-A1, 2005.
45. Nag, M.; Basak, P.; Manorama, S. V. Low Temperature Hydrothermal Synthesis of Phase-Pure Rutile Titania Nanocrystals: Time Temperature Tuning of Morphology and Photocatalytic Activity. *Mater. Res. Bull.* **2007**, *42*, 1691–1704.
46. Armstrong, A. R.; Armstrong, G.; Canales, J.; Garcìa, R.; Bruce, P. G. Lithium-Ion Intercalation into TiO_2-B Nanowires. *Adv. Mater.* **2005**, *7*, 862–865.
47. Kasuga, T.; Hiramatsu, M.; Hoson, A.; Sekino, T.; Niihara, K. Titania Nanotubes Prepared by Chemical Processing. *Adv. Mater.* **1999**, *11*, 1307–1311.
48. Kasuga, T.; Hiramatsu, M.; Hoson, A.; Sekino, T.; Niihara, K. Formation of Titanium Oxide Nanotube. *Langmuir* **1998**, *14*, 3160–3163.
49. Pottier, A.; Chanéac, C.; Tronc, E.; Mazerolles, L.; Jolivet, J.-P. Synthesis of Brookite TiO_2 Nanoparticles by Thermolysis of $TiCl_4$ in Strongly Acidic Aqueous Media. *J. Mater. Chem.* **2001**, *11*, 1116–1121.
50. Zhang, S.; Peng, L. M.; Chen, Q.; Du, G. H.; Dawson, G.; Zhou, W. Z. Formation Mechanism of $H_2Ti_3O_7$ Nanotubes. *Phys. Rev. Lett.* **2003**, *91*, 256103-1–256103-4.
51. Yao, B. D.; Chan, Y. F.; Zhang, X. Y.; Zhang, W. F.; Yang, Z. Y.; Wang, N. Formation Mechanism of TiO_2 Nanotubes. *Appl. Phys. Lett.* **2003**, *82*, 281–283.
52. Sun, X.; Li, Y. Synthesis and Characterization of Ion-Exchangeable Titanate Nanotubes. *Chem.—Eur. J.* **2003**, *9*, 2229–2238.
53. Yang, J.; Jin, Z.; Wang, X.; Li, W.; Zhang, J.; Zhang, S.; Guo, X.; Zhang, Z. Study on Composition, Structure and Formation Process of Nanotube $Na_2Ti_2O_4(OH)_2$. *Dalton Trans.* **2003**, 3898–3901.
54. Du, G. H.; Chen, Q.; Che, R. C.; Yuan, Z. Y.; Peng, L. M. Preparation and Structure Analysis of Titanium Oxide Nanotubes. *Appl. Phys. Lett.* **2001**, *79*, 3702–3704.
55. Tsai, C. C.; Teng, H. Structural Features of Nanotubes Synthesized from NaOH Treatment on TiO_2 with Different Post-Treatments. *Chem. Mater.* **2006**, *18*, 367–373.
56. Sekino, T. Synthesis and Applications of Titanium Oxide Nanotubes. In *Inorganic and Metallic Nanotubular Materials*; Kijima, T., Ed.; Springer-Verlag: Berlin, 2010; Topics in Applied Physics Vol. 117, pp 17−32.
57. Wang, Z. L. Transmission Electron Microscopy of Shape-Controlled Nanocrystals and Their Assemblies. *J. Phys. Chem. B* **2000**, *104*, 1153–1175.
58. Maiyalagan, T.; Viswanathan, B.; Varadaraju, U. V. Fabrication and Characterization of Uniform TiO_2 Nanotube Arrays by Sol−Gel Template Method. *Bull. Mater. Sci.* **2006**, *29*, 705–708.
59. Armstrong, A. R.; Armstrong, G.; Canales, J.; Bruce, P. G. TiO_2-B Nanowires. *Angew. Chem., Int. Ed.* **2004**, *43*, 2286–2288.
60. Murciano, L. T.; Lapkin, A. A.; Chadwick, D. Synthesis of High Aspect Ratio Titanate Nanotubes. *J. Mater. Chem.* **2010**, *20*, 6484–6489.
61. Ratanatawanate, C.; Xiong, C.; Kenneth, J.; Balkus, Jr. Fabrication of PbS Quantum Dot Doped TiO_2 Nanotubes. *ACS Nano* **2008**, *2*, 1682–1688.
62. Qiana, L.; Dub, Z. L.; Yanga, S. Y.; Jin, Z. S. Raman Study of Titania Nanotube by Soft Chemical Process. *J. Mol. Struct.* **2005**, *749*, 103–107.
63. Maxim, F.; Ferreira, P.; Vilarinho, P. M. Influence of the Neutralization Process on the Preparation of Titanate Nanotubes by Hydrothermal Synthesis. *J. Porous Mater.* **2011**, *18*, 37–45.
64. Rajh, T.; Chen, L. X.; Lukas, K.; Liu, T.; Thurnauer, M. C.; Tiede, D. M. Surface Restructuring of Nanoparticles: An Efficient Route for Ligand−Metal Oxide Crosstalk. *J. Phys. Chem. B* **2002**, *106*, 10543–10552.
65. Dimitrijevic, N. M.; Saponjic, Z. V.; Bartels, D. M.; Thurnauer, M. C.; Tiede, D. M.; Rajh, T. Revealing the Nature of Trapping Sites in Nanocrystalline Titanium Dioxide by Selective Surface Modification. *J. Phys. Chem. B* **2003**, *107*, 7368–7375.
66. Moser, J.; Punchihewa, S.; Infelta, P. P.; Graetzel, M. Surface Complexation of Colloidal Semiconductors Strongly Enhances Interfacial Electron-Transfer Rates. *Langmuir* **1991**, *7*, 3012–3018.
67. McWhirter, M. J.; Bremer, P. J.; Lamont, I. L.; McQuillan, A. J. Siderophore-Mediated Covalent Bonding to Metal (Oxide) Surfaces during Biofilm Initiation by *Pseudomonas aeruginosa* Bacteria. *Langmuir* **2003**, *19*, 3575–3577.
68. Niederberger, M.; Garnweitner, G.; Krumeich, F.; Nesper, R.; Cölfen, H.; Antonietti, M. Tailoring the Surface and Solubility Properties of Nanocrystalline Titania by a Nonaqueous *In Situ* Functionalization Process. *Chem. Mater.* **2004**, *16*, 1202–1208.
69. Chen, L.; Rahme, K.; Holmes, J. D.; Morris, M. A.; Slater, N. K. H. Non-Solvolytic Synthesis of Aqueous Soluble TiO_2 Nanoparticles and Real-Time Dynamic Measurements of the Nanoparticle Formation. *Nanoscale Res. Lett.* **2012**, *7*, 297-1–297-10.
70. Araujo, P. Z.; Morando, P. J.; Blesa, M. A. Interaction of Catechol and Gallic Acid with Titanium Dioxide in Aqueous Suspensions. 1. Equilibrium Studies. *Langmuir* **2005**, *21*, 3470–3474.
71. Balamurugan, S. S.; Cantu, E. S.; Cueto, R.; Russo, P. S. Preparation of Organosoluble Silica-Polypeptide Particles by "Click" Chemistry. *Macromolecules* **2010**, *43*, 62–70.
72. Bartholome, C.; Beyou, E.; Lami, B. E.; Chaumont, P.; Zydowicz, N. Nitroxide-Mediated Polymerizations from Silica Nanoparticle Surfaces: "Graft from" Polymerization of Styrene Using a Triethoxysilyl-Terminated Alkoxyamine Initiator. *Macromolecules* **2003**, *36*, 7946–7952.
73. MacDonald, J. R.; Johnson, W. B. In *Impedance Spectroscopy*; MacDonald, J. R., Ed.; J. Wiley & Sons: New York, 1987; p 23.
74. Lasia, A. Electrochemical Impedance Spectroscopy and Its Applications. In *Modern Aspects of Electrochemistry*; Conway, B. E., Bockris, J., White, R. E., Eds.; Kluwer Academic/Plenum Publishers: New York, 1999; Vol. 32, pp 143−248.
75. MacDonald, J. R. Impedance Spectroscopy. *Ann. Biomed. Eng.* **1992**, *20*, 289–305.
76. Karthikeyan, A.; Vinatier, P.; Levasseur, A. Study of Lithium Glassy Solid Electrolyte/Electrode Interface by Impedance Analysis. *Bull. Mater. Sci.* **2000**, *23*, 179–183.
77. Sinclair, D. C. Characterization of Electro-Materials Using AC Impedance Spectroscopy. *Bol. Soc. Esp. Ceram. Vidrio* **1995**, *34*, 55–65.
78. Jennings, J. R.; Wang, Q. Influence of Lithium Ion Concentration on Electron Injection, Transport, and Recombination in Dye-Sensitized Solar Cells. *J. Phys. Chem. C* **2010**, *114*, 1715–1724.
79. Sakai, N.; Ebina, Y.; Takada, K.; Sasaki, T. Electronic Band Structure of Titania Semiconductor Nanosheets Revealed by Electrochemical and Photoelectrochemical Studies. *J. Am. Chem. Soc.* **2004**, *126*, 5851–5858.
80. Chernatynskiy, A.; Clarke, D. R.; Phillpot, S. R. Thermal Transport in Nanostructured Materials. In *Handbook of Nanoscience, Engineering, and Technology*; Goddard, W. A., III, Brenner, D., Lyshevski, S. E., Iafrate, G. J., Eds.; CRC Press: Boca Raton, FL, 2012; pp 545−572.
81. Stroscio, M. A.; Dutta, M. In *Phonons in Nanostructures*; Cambridge University Press, Cambridge, U.K., 2001.

82. Basak, P.; Manorama, S. V.; Singh, R. K.; Prakash, O. Investigations on the Mechanisms of Ionic Conductivity in PEO–PU/PAN Semi-Interpenetrating Polymer Network–Salt Complex Polymer Electrolytes: An Impedance Spectroscopy Study. *J. Phys. Chem. B* **2005**, *109*, 1174–1182.
83. Di Noto, V.; Vittadello, M.; Lavina, S.; Fauri, M.; Biscazzo, S. Mechanism of Ionic Conductivity in Poly(ethylene glycol 400) $(LiCl)_x$ Electrolytes Complexes: Studies Based on Electrical Spectroscopy. *J. Phys. Chem. B* **2001**, *105*, 4584–4595.
84. Roling, B.; Martiny, C.; Funke, K. Information on the Absolute Length on Scales of Ion Transport Processes in Glasses from Electrical Conductivity and Tracer Diffusion Data. *J. Non-Cryst. Solids* **1999**, *249*, 201–209.
85. Roling, B. What do Electrical Conductivity and Electrical Modulus Spectra Tell Us About the Mechanism of Ion Transport Processes in Melts, Glasses and Crystals? *J. Non-Cryst. Solids* **1999**, *244*, 34–43.
86. Furukawa, T.; Imura, M.; Yuruzume, H. Broad-Band Conductive Spectra of Polypropylene Oxide Complexed with $LiClO_4$. *Jpn. J. Appl. Phys.* **1997**, *36*, 1119–1125.
87. Furukawa, T.; Yoneya, K.; Takahashi, Y.; Ito, K.; Ohno, H. Correlation Between Ionic and Dipolar Motions in a Single Ion Conducting Polymer P[MEO_9MAM]. *Electrochim. Acta* **2000**, *45*, 1443–1448.
88. Di Noto, V. Electrical Spectroscopy Studies of Lithium and Magnesium Polymer Electrolytes based on PEG 400. *J. Phys. Chem. B* **2002**, *106*, 11139–11154.
89. Di Noto, V. Zeolite Organic-inorganic Polymer Electrolytes Based on Oligo(ethylene glycol) 600 K_2PdCl_4 and $K_3Co(CN)_6$. *J. Phys. Chem. B* **2000**, *104*, 10116–10125.
90. Jonscher, A. K. The Universal Dielectric Response. *Nature* **1977**, *267*, 673–679.
91. Crammer, C.; Funke, K.; Seatkamp, T.; Wilmer, D.; Ingram, M. D. Conductivity and Spectroscopy. *Z. Naturforsch., A: Phys. Sci.* **1995**, *50*, 613–623.